Available online at www.sciencedirect.com
ScienceDirect
Journal of the European Ceramic Society 27 (2007) 3413–3424
www.elsevier.com/locate/jeurceramsoc

Preparation by solar physical vapor deposition (SPVD) and nanostructural study of pure and Bi doped ZnO nanopowders

T. Ait Ahcene [a,b], C. Monty [a,*], J. Kouam [a], A. Thorel [c], G. Petot-Ervas [d], A. Djemel [e]

[a] *Laboratoire CNRS/PROMES, Odeillo 66120 Font Romeu, France*
[b] *Département de Physique, Faculté des Sciences, Université Mouloud Mammeri, Tizi Ouzou 15000, Algeria*
[c] *Laboratoire des Matériaux de l'ENSMP, 91003 Evry, France*
[d] *Laboratoire SPMS, CNRS-CEA, Ecole Centrale Paris, Chatenay-Malabry, France*
[e] *Laboratoire de physique chimie des Semiconducteurs, Université Mentouri, Constantine 25000, Algeria*

Received 26 August 2006; received in revised form 22 December 2006; accepted 8 January 2007
Available online 5 April 2007

Abstract

Pure and Bi doped ZnO nanopowders have been prepared by a physical vapor deposition process in a solar reactor (SPVD). From X-ray diffraction (XRD) spectra performed on initial targets and on the nanopowders obtained, the lattice parameters and the phase changes as well as the average grain sizes and the grain shape anisotropies have been determined. High Resolution Transmission Electron Microscopy (HRTEM) observations support the results. The pure ZnO nanopowders "grain size" and "grain shape anisotropy" (whiskers with an average diameter of 20–40 nm) is a function of the air pressure during the vaporisation–condensation process: the higher the pressure, the longer the whiskers. The bismuth doped ZnO nanopowders are polyphased but the ZnO based majority phases behave similarly to pure ZnO with a tendency to form whiskers but with a grain size and grain shape anisotropy decreasing when the Bi content increases.

Preliminary electrical measurements at temperatures below 300 °C have shown that the ionic conductivity of the nanocomposites obtained starting from ZnO + 23 wt% Bi_2O_3 targets is high and promising for applications.

Keywords: Powders-gas phase reaction; ZnO; Nanocomposites; Electrical conductivity; Nanopowders

1. Introduction

Zinc oxide (ZnO) is a material which has been extensively studied because of its use in a wide range of applications related to its chemical and physical properties. ZnO is used as transparent conductive electrodes.[1,2] In optoelectronics, ZnO is a promising material for the fabrication of blue light emitting diodes.[3,4] It is also the best substrate available for the epitaxy of GaN layers.[5] It is used in chemistry and catalysis for its surface properties and its chemical reactivity (synthesis of methanol,[6,7] stabilisation of polyethylene,[8] pollutant degradation,[9] ...). The main aim in this work is the manufacture of doped zinc oxide varistors used for the protection of electric or electronic devices against the voltage surge.[10–13] This application depends on the microstructure, it is based on the electrical conductivity of the bulk, of the grain boundaries and of the interfaces between the solid solution $Zn_{1-x}Bi_xO_{1-\delta}$ and secondary phases.[14] The greater the number of the grain boundaries in the material, the more significant is the varistor effect. This effect is due to potential barriers related to the segregation or the precipitation of added elements, such as bismuth, to the grain boundaries. Consequently, zinc oxide ultrafine powders have been prepared to increase the number of the grain boundaries and of the potential barriers in the massive nanomaterials.[15,16] However, the evaporation of bismuth oxide during sintering, which leads to a porous material of very low density,[17,18] remains the major disadvantage of the addition of this oxide alone, essential to the varistor effect.

In this work, pure and Bi_2O_3 doped ZnO nanopowders of different grain sizes have been prepared. The powder nanostructure was characterized and studied using various techniques including X-ray Diffraction (XRD) and High Resolution Transmission Electron Microscopy (HRTEM).

* Corresponding author.
E-mail address: monty@promes.cnrs.fr (C. Monty).

0955-2219/$ – see front matter © 2007 Elsevier Ltd. All rights reserved.
doi:10.1016/j.jeurceramsoc.2007.01.020

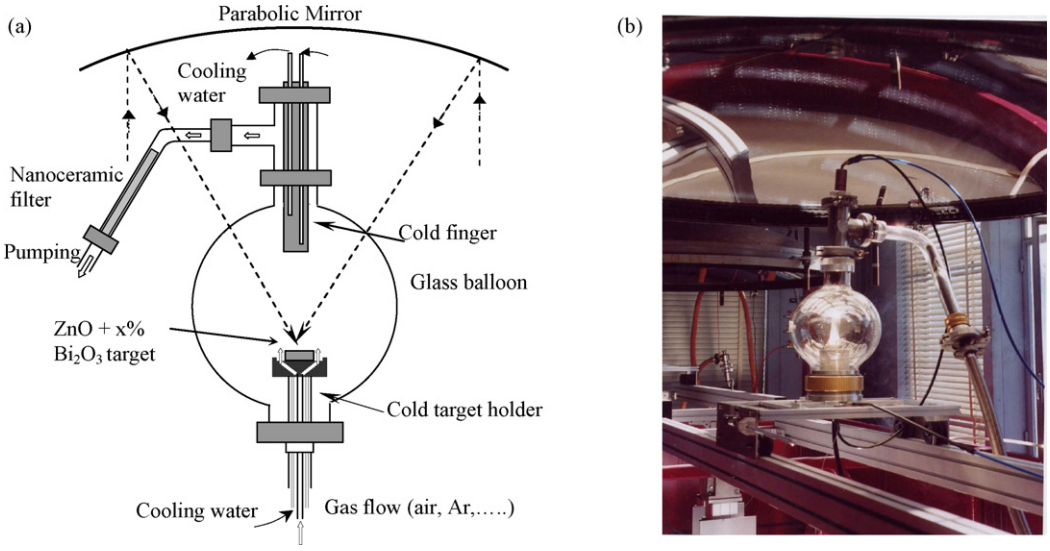

Fig. 1. (a) Solar physical vapor deposition (SPVD) process in the "heliotron" solar reactor and (b) view of the "heliotron" solar reactor.

2. Experimental

2.1. Nanopowders preparation by the SPVD process

The zinc oxide based ultrafine powders were prepared by vaporisation–condensation in a solar reactor (solar physical vapor deposition or SPVD). This method consists, to sublimate pure ZnO (Johnson&Matthey) or Bi_2O_3 doped ZnO by concentrating the solar radiation on targets made of compacted powder.[19,20] The nanopowders are collected by scraping the deposit formed on a cold finger (water cooled copper tube), or by trapping them on a nanoceramic filter through which the smokes produced are pumped. Fig. 1a and b shows the more recent solar reactor of this type, called "heliotron". Pure zinc oxide nanopowders were prepared under various pressures of air in the solar reactor ($P = 5$, 30, 70 and 100 Torr). The Bi doped targets used in this study have been prepared by mixing ZnO and Bi_2O_3 powders with several compositions (1, 5, 12 and 20 wt% Bi_2O_3, corresponding, respectively, to 0.176, 0.911, 2.326, 4.183 mol% Bi_2O_3). After mixing, the powders were compacted and annealed at 700 °C under air during more than 2 h. The microstructural study of these targets is detailed in Section 3.2.2.

2.2. Characterization methods

Crystalline powder structure was recorded by X-ray diffraction with Cu Kα radiation ($\lambda = 1.54056$ Å) using a Philips diffractometer. Each diffraction peak was deconvoluted by two Lorentz functions each one corresponding to the radiations $\lambda_{K\alpha1}$ (1.540656) and $\lambda_{K\alpha2}$ (1.54438) of Cu (ORIGIN 6.0 software). The spectra were scanned over the 2θ angular range 10–70°.

From XRD peaks width it is possible to determine an "average grain size" (in fact the "coherent diffraction domains" average size)[30] of the nanopowders by applying the Scherrer formula to

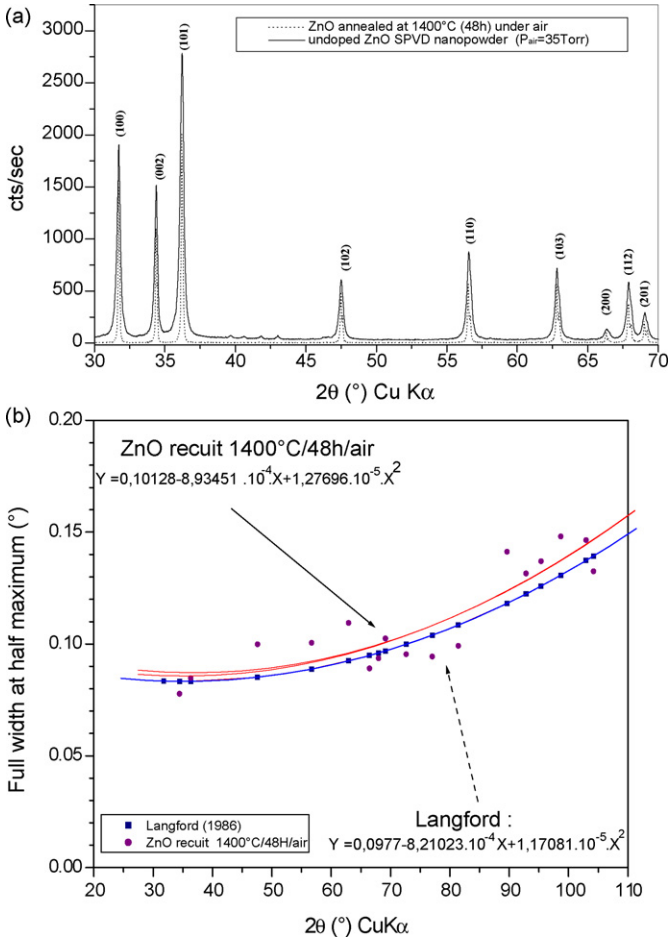

Fig. 2. (a) XRD spectra of a pure ZnO nanopowder prepared by SPVD compared with commercial ZnO annealed at 1400 °C during 48 h under air. (b) XRD width determined on ZnO annealed at 1400 °C/48 h/air and compared with the "instrumental width" determined by Langford and coworkers.[30]

XRD diffraction peaks[28,29]:

$$d_m = \frac{K\lambda}{\delta_{cor}\cos\theta} = \frac{0.9\lambda}{\delta_{cor}\cos\theta}$$

where d_m is the mean crystallite size in the considered *hkl* direction, λ the wavelength (Cu Kα), θ the Bragg diffraction angle and δ_{cor} is the corrected half-width of the diffraction peak.

In this study the peak shape was nearly Gaussian and it was considered that:

$$\delta_{cor} = (w^2 - w_{st}^2)^{1/2}$$

where w is the experimental width at half-peak intensity or Full Width at Half Maximum (FWHM) in radians, related to the nanopowder and w_{st} is the "instrumental width".

We have determined the instrumental width from XRD spectra of well-annealed pure ZnO, it obeyed in this series of experiments to the relation:

$$y = 0.101 - 8.93 \times 10^{-4}x + 1.28 \times 10^{-5}x^2$$

where x stands for 2θ in degrees and y is also in degrees. This function was found quite close to the function proposed by Langford[29,30] (see Fig. 2b).

3. Results

3.1. Structural study of undoped ZnO nanopowders

XRD spectra performed on undoped ZnO nanopowders obtained by the SPVD process and annealed ZnO commercial powder are shown in Fig. 2. As a first approximation, they are in agreement with literature data for pure ZnO (JCPDS no. 80-0075: zincite hexagonal structure, $a = b = 3.25$ Å, $c = 5.21$ Å, spatial group $P6_3mc$).

Fig. 3 shows the XRD diagram as a function of the pressure inside the reactor during the SPVD process ($P = 5$, 30, 70 and 100 Torr). From these spectra, the lattice parameters and cell volume variations of pure ZnO nanopowders have been determined (see Fig. 17 later). It can be noticed that the lattice parameter a is nearly constant while the parameter c increases with the air

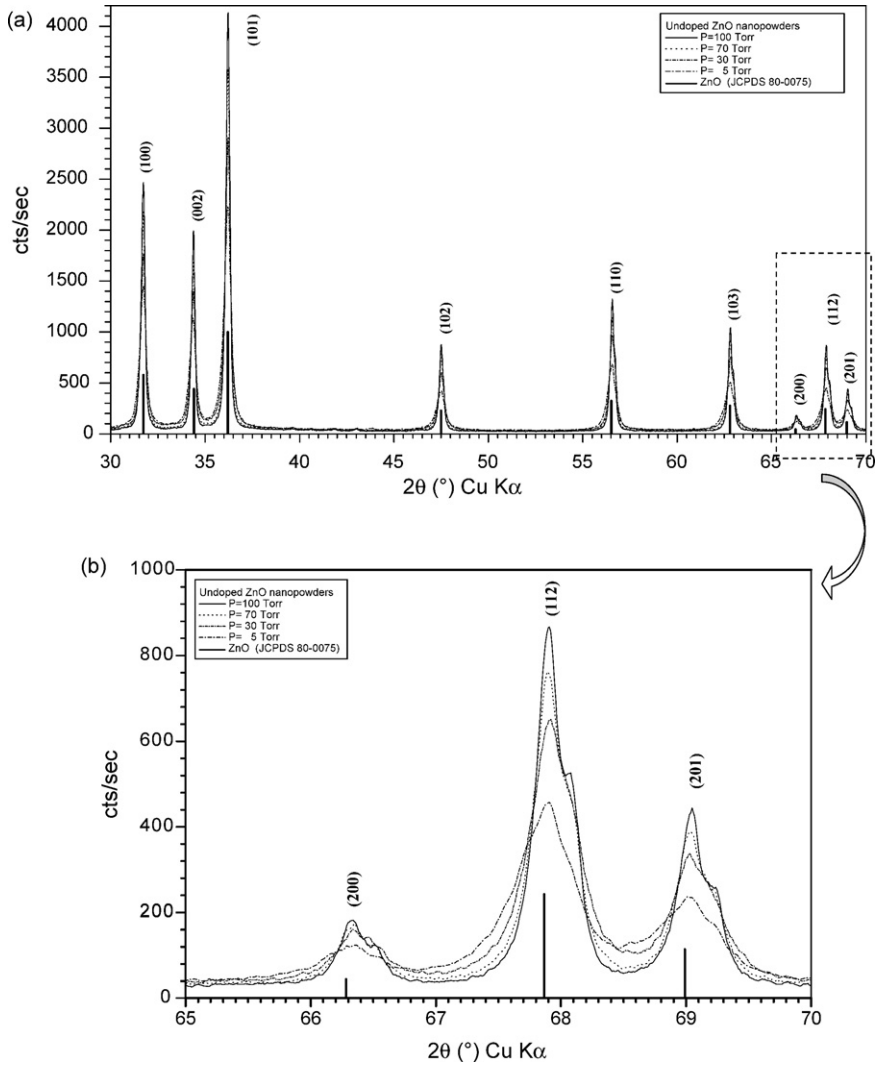

Fig. 3. (a) Evolution of the undoped ZnO nanopowders XRD spectra as a function of the air pressure during the preparation by the SPVD process. (b) Evolution of 2 0 0, 1 1 2 and 2 0 1 XRD peak shape and position as a function of the air pressure during the undoped ZnO nanopowders preparation by the SPVD process.

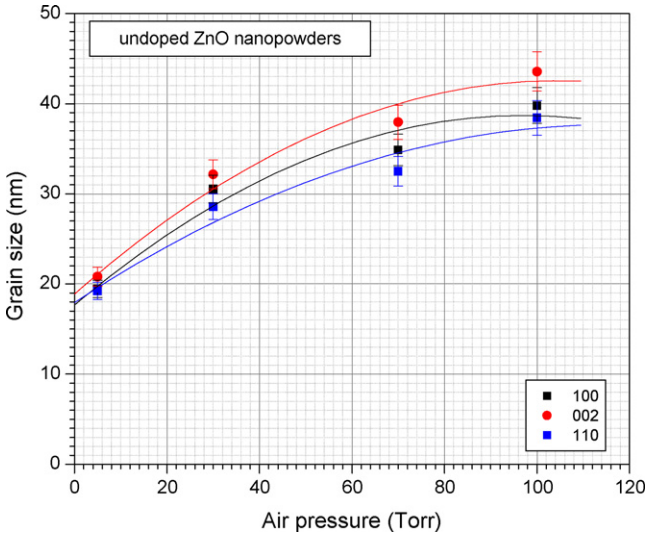

Fig. 4. Grain size of undoped zinc oxide nanopowders as a function of the air pressure during the SPVD process.

pressure and consequently, that the volume of the elementary cell increases, remaining larger than the volume deduced from XRD data. Comparing the experimental values obtained in this study to the literature data it appears that the best agreement is obtained with (JCPDS 80-0075) determinated also on ZnO nanopowders[31] and that the values of the c parameter are higher than most of the literature data.

From XRD peaks broadening (see, for example, Fig. 3b) the average "grain size" of the powders has been determined as a function of the air pressure (see Fig. 4): the lower the pressure, the smaller the particles. A striking result is that the grain size is dependent on the crystallographic (1 0 0, 1 1 0, 0 0 2) directions. Transmission Electron Microscopy observations show also that when the air pressure increases, the structure varies from smaller and isotropic grains to whiskers (often four of them are linked as "tetrapods",[32–36] see Fig. 5); this shape anisotropy can explain the observed crystallographic dependency of the average grain size.

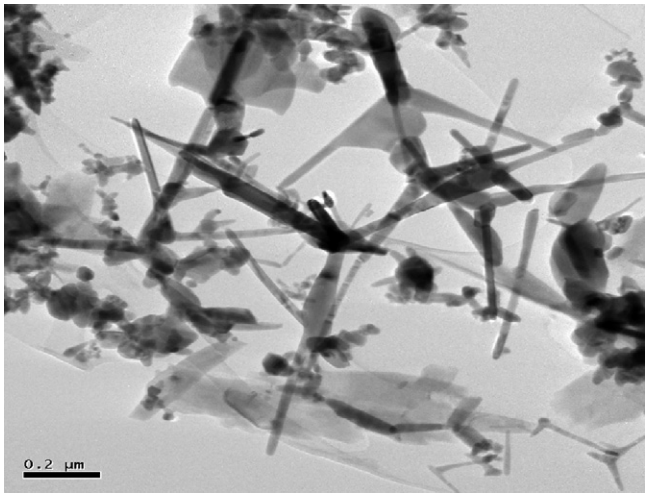

Fig. 5. TEM observations on undoped ZnO nanopowders: whiskers and precipitates are visible simultaneously.

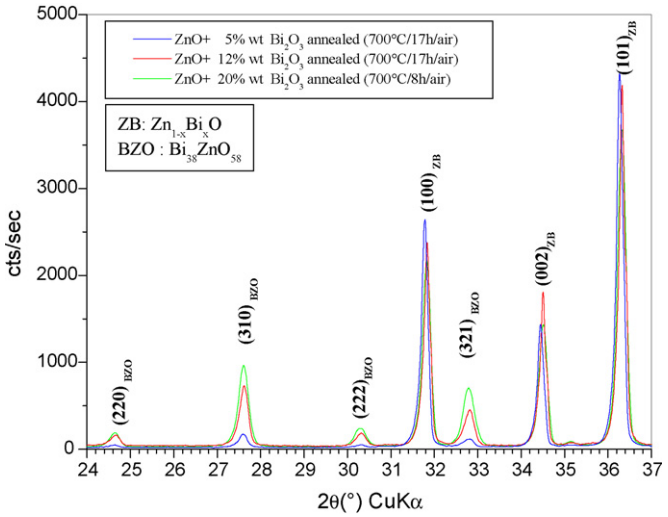

Fig. 6. XRD spectra of Bi doped ZnO targets annealed at 700 °C during more than 2 h in air.

3.2. Structural study of Bi_2O_3 doped ZnO nanopowders

3.2.1. Initial powders

XRD spectra have been performed on Bi_2O_3 doped ZnO initial powders used to prepare targets for the SPVD process (see Fig. 6). After annealing during more than 2 h at 700 °C in air in such a way the solid-state reactions were achieved and the activity of the bismuth oxide reduced a solid solution $Zn_{1-x}Bi_xO$, close to pure ZnO (ref. JCPDS 80-075) was found both with the cubic phase $Bi_{38}ZnO_{58+\delta}$ ($\delta = 0$, ref. JCPDS 42-183; $\delta = 2$, ref. JCPDS 41-0253), according to published phase diagrams (see Appendix A). The formula of this cubic compound can also be written as $(Bi_{1-0.025}Zn_{0.025})_2O_{3-0.1}$ and is considered as close to γ-Bi_2O_3. The peak intensities corresponding to the $Bi_{38}ZnO_{58+\delta}$ phase increase with the Bi content in the sample, while the peak intensities corresponding to the solid solution $Zn_{1-x}Bi_xO$ only slightly vary.

3.2.2. Bi_2O_3 doped ZnO nanopowders

Nanopowders were obtained by the SPVD process in air (air pressure was 30–40 Torr). Their XRD diagrams are seen in Fig. 7. A solid solution $Zn_{1-y}Bi_yO$ ($y \neq x$) whose XRD peaks are slightly shifted to the high angles (comparing to pure ZnO) has been found. Beside $Zn_{1-y}Bi_yO$, the phase $Bi_{7.65}Zn_{0.35}O_{11.83}$ has been also identified (ref. JCPDS 43-0449). The phase $Bi_{7.65}Zn_{0.35}O_{11.83}$ is in fact a Bi rich solid solution whose tetragonal structure is similar to that of β-Bi_2O_3 (ref. JCPDS 78-1793) considered by most of the authors as a metastable phase.[21,22] The formula can also be written considering an interstitial solid solution: $Bi_{2-u}Zn_{u/2}O_{3-u/2}$ with $u = 0.0875$.

The XRD spectra obtained on Bi_2O_3 doped ZnO nanopowders at different compositions (see Fig. 7) show that diffraction peaks are shifted to the high angles when the Bi concentration increases. Fig. 8 is a detailed view of the spectra obtained on 12 wt% Bi_2O_3 doped ZnO target and on the nanopowder obtained from this target by the SPVD process (its composition has been determined by X-ray Fluorescence to be in average

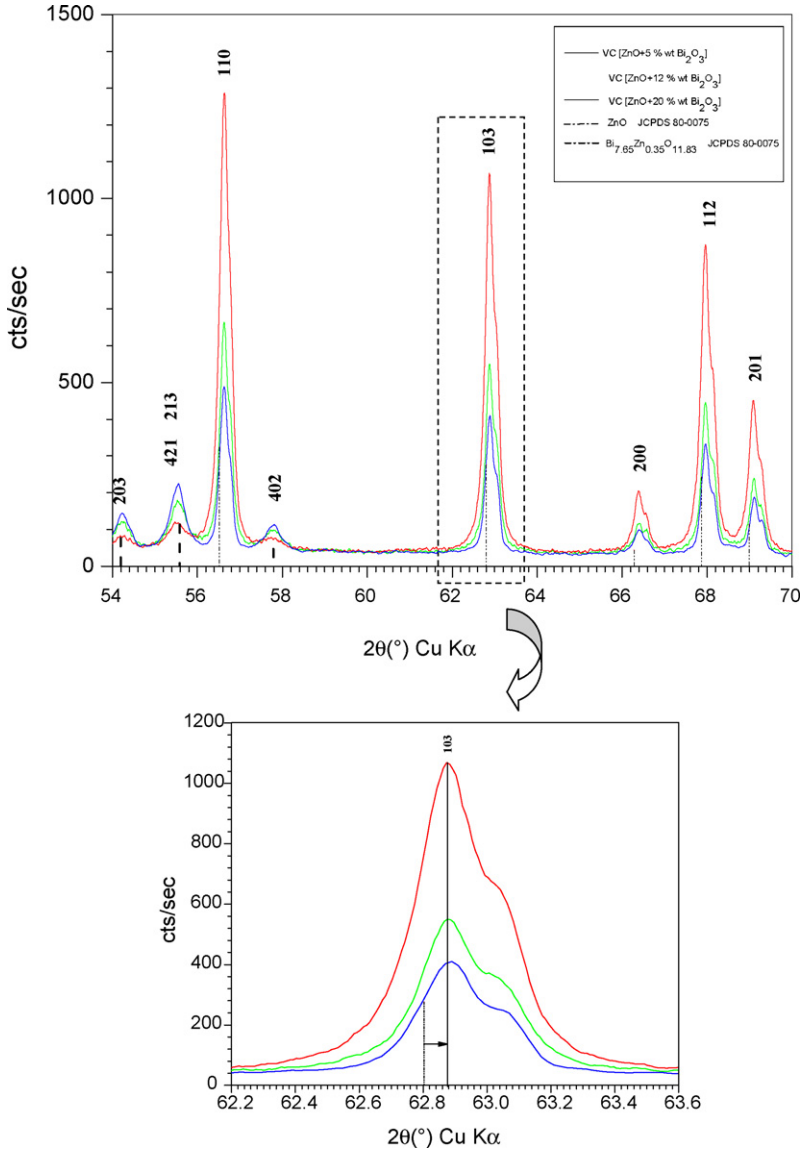

Fig. 7. XRD spectrum obtained at different Bi content in ZnO nanopowders (the noted composition refers to the initial composition of the target).

18 wt% Bi_2O_3). Fig. 9 shows that the dependency of the final composition c_f (in wt% Bi_2O_3) varies linearly with the initial composition c_i (in wt% Bi_2O_3) following a law which can be written: $c_f = 1.5c_i$. The parameter x has also been reported in Table 1 (x is obtained writing the oxide mixtures of Bi_2O_3 and ZnO as a fictive solid solution $Zn_{1-x}Bi_xO$).

As seen in Table 1 and Fig. 9, the nanopowders are more Bi rich than the targets.

The parameters a or b and c, as well as the cell volume, computed from the XRD spectra (such as those shown in Fig. 7) have been reported in Fig. 10a–c. The parameters a or b are practically unchanged while the c parameter is practically independent on the Bi content and is strongly lowered compared to the literature data for pure ZnO, to annealed ZnO powders and to the pure ZnO nanopowders. As a consequence, the cell volume is also lowered.

Table 1
Composition of the nanopowders as a function of the composition of the targets used in the SPVD process (average values have been reported both in weight % and in atomic fraction)

Bi_2O_3 content of targets (wt%)	Bi average content of targets (x in $Zn_{1-x}Bi_xO$)	Bi_2O_3 average content of nanopowders (wt%)	Bi average content of nanopowders (x in $Zn_{1-x}Bi_xO$)
1.5	0.00352	3.518	0.01257
5	0.01805	6.656	0.0243
10	0.0373	18.47	0.07332
20	0.0803	30.613	0.13352
30	0.1302	44.437	0.21834

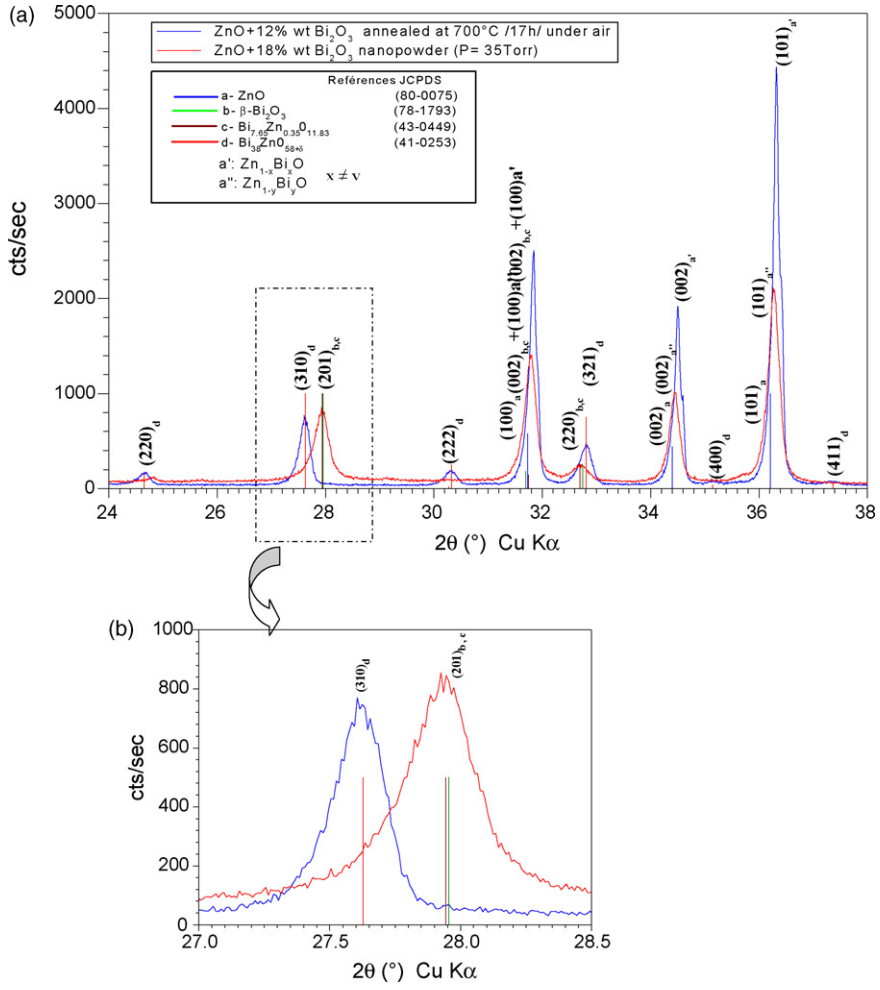

Fig. 8. (a) XRD spectra of a 12 wt% Bi_2O_3 doped ZnO before and after SPVD. The indices a–d in the diagram indicate the various phases. (b) Zoom of a around $2\theta = 28°$.

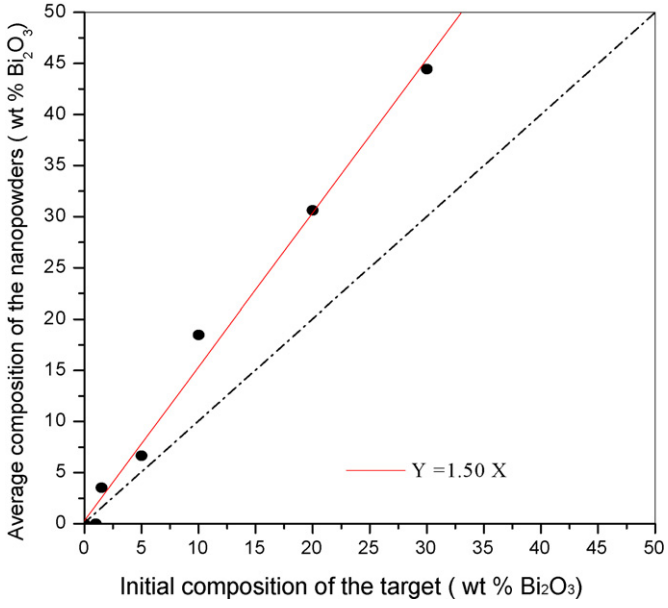

Fig. 9. Average Bi_2O_3 content of nanopowders prepared by SPVD as a function of the target Bi_2O_3 average content (wt%).

The grain size of the $Zn_{1-y}Bi_yO$ majority phase has been deduced from the XRD diagrams following the procedure described in Section 2.2. The results obtained on peaks 1 0 0, 0 0 2 and 1 0 1 are reported in Fig. 11. As seen in this figure, the "grain size" of the solid solution $Zn_{1-y}Bi_yO$ is decreasing when the Bi_2O_3 content of the targets is increasing. The grain size depends on the crystallographic orientation: monocrystalline grains are elongated along the *c*-axis. This anisotropy of shape seems to be less important at high bismuth content. Transmission Electron Microscopy observations and HRTEM are in agreement with the XRD analysis: many whiskers appear in undoped and slightly doped nanopowders prepared by SPVD; increasing the bismuth content, the morphology changes from whiskers to more compact shapes (see Figs. 12–14).

3.3. Electrical properties

One of the aims of this study was to prepare Bi doped ZnO nanomaterials and to investigate their electrical properties. Two kinds of samples were prepared:

- Pellets of 13 mm in diameter of 23 wt% Bi_2O_3 doped ZnO nanopowders (obtained from a 15 wt% Bi_2O_3 doped ZnO

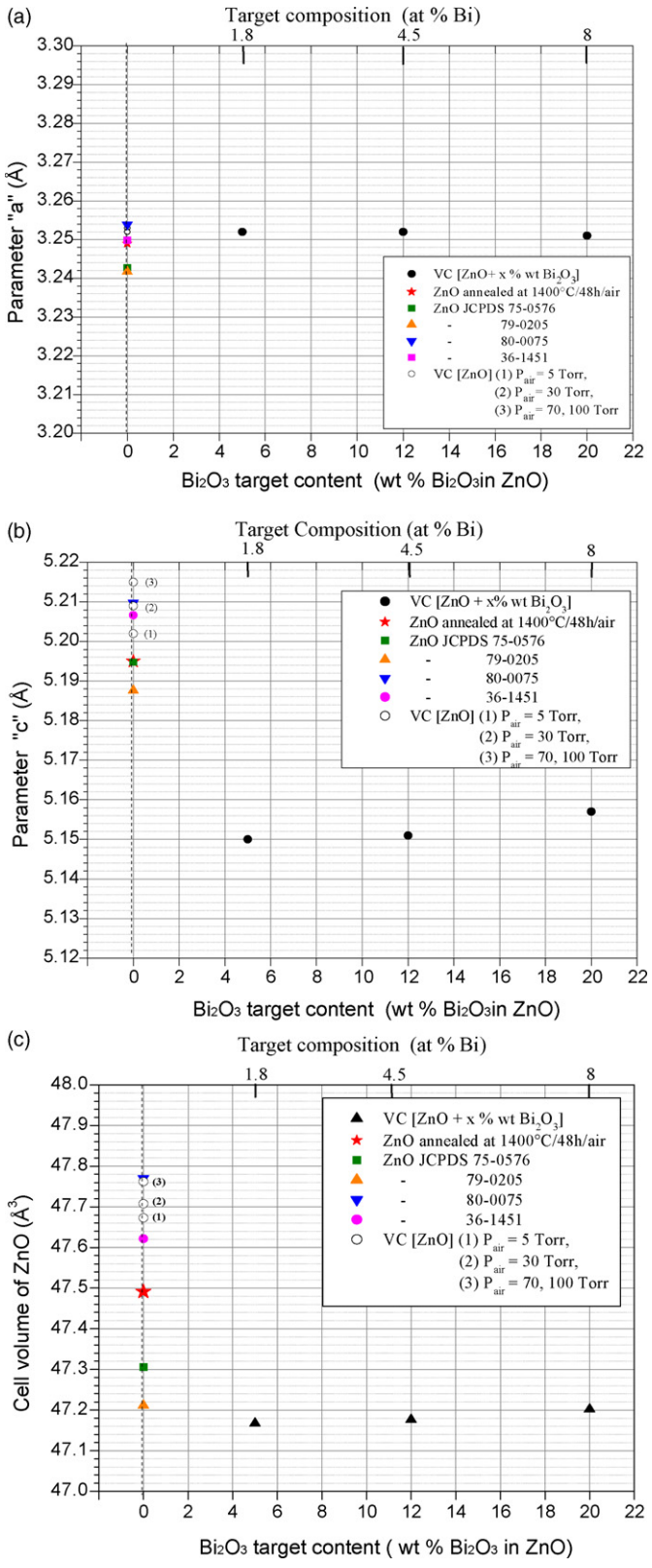

Fig. 10. (a) *a* parameter variation of the solid solution $Zn_{1-x}Bi_xO$ in the nanopowders as a function of Bi_2O_3 total content of the target. (b) *c* parameter variation of the solid solution $Zn_{1-x}Bi_xO$ in the nanopowders as a function of Bi_2O_3 total content of the target. (c) Volume of the unit cell of $Zn_{1-x}Bi_xO$ as a function of the Bi_2O_3 content of the target.

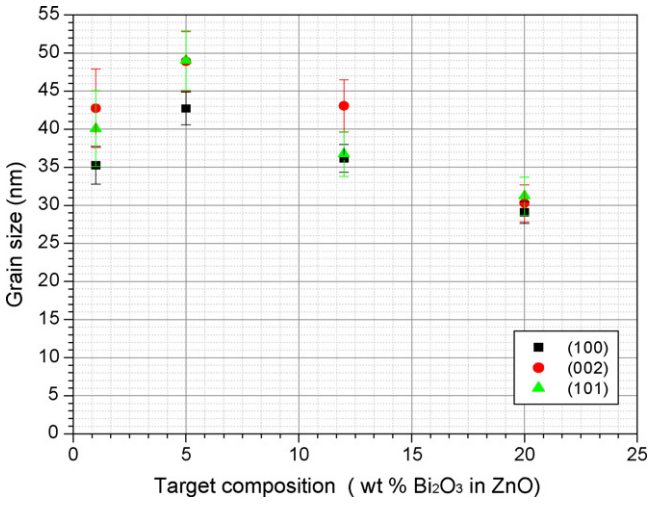

Fig. 11. Influence of bismuth oxide content of the targets on the grain size of the nanopowders.

target), pressed at 75 MPa and annealed at 700 °C in air for 2 h. The density of the sample after sintering was 5.8 (measured by Archimede method and estimated to be 97.7% of the theoretical density). Sintering of 23 wt% Bi_2O_3 doped ZnO nanopowders at 800 °C under air during 2 h lead to the apparition of a phase $(Bi_{1-z}Zn_z)_2O_3$ very close to α-Bi_2O_3 (monoclinic, JCPDS no. 71-2274) beside the solid solution $Zn_{1-y'}Bi_{y'}O$.

- The $Bi_{38}ZnO_{58+\delta}$ compound has been synthesized to know more about its structure and properties, specially electrical properties (see Section 3.3). The preparation of the phase $Bi_{38}ZnO_{58+\delta}$ was carried out by mixing 1 mole ZnO with 19 moles of Bi_2O_3. The powder mixture was compacted at 200 MPa, sintered at 700 °C during 12 h and annealed again at 730 °C during 5 h under air to obtain a pellet of density around 83%.

XRD analysis indicates (see Fig. 15) that only this phase appears.

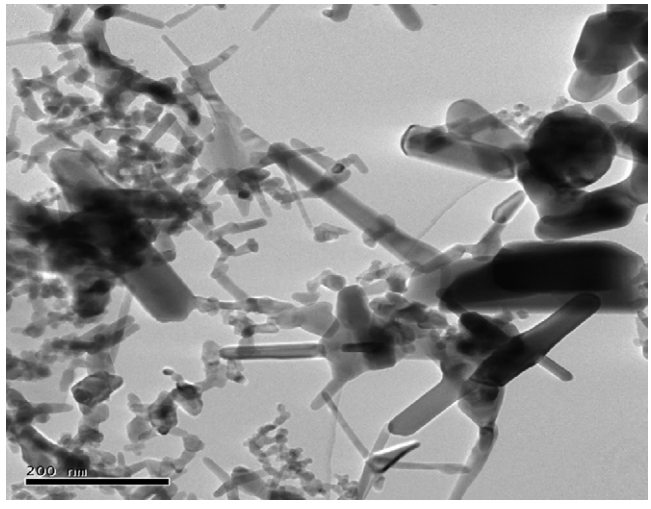

Fig. 12. TEM images of nanopowders prepared by the SPVD method at air pressure $P = 15$ Torr for 5 wt% Bi_2O_3 in ZnO targets.

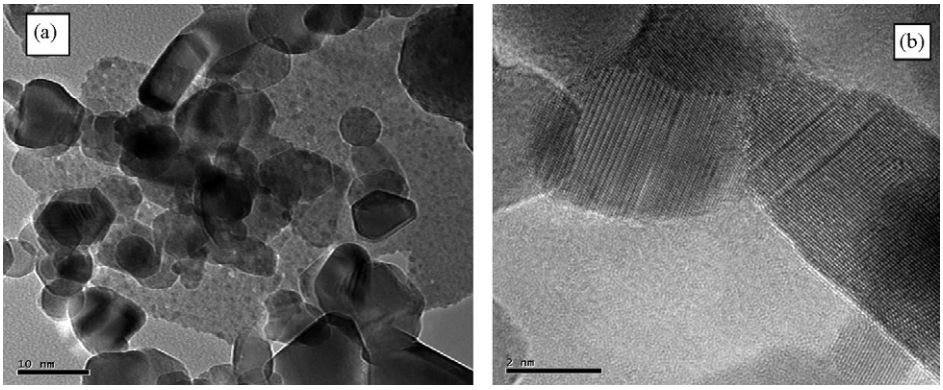

Fig. 13. (a) TEM images of nanopowders prepared by SPVD at air pressure $P = 20$ Torr for 10 wt% Bi_2O_3 doped ZnO targets. (b) HRTEM images nanopowders prepared by SPVD at air pressure $P = 20$ Torr for 10 wt% Bi_2O_3 doped ZnO targets.

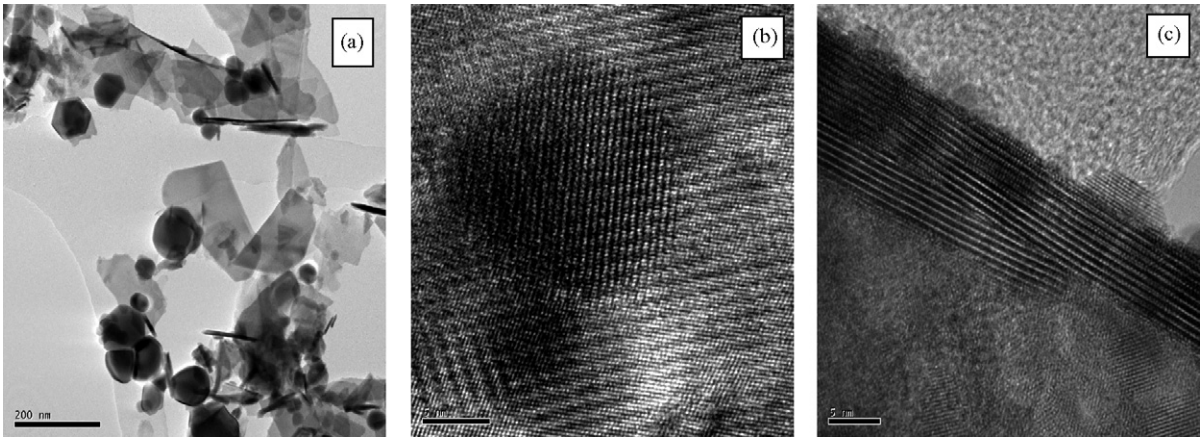

Fig. 14. (a) TEM images of nanopowders prepared by SPVD at air pressure $P = 20$ Torr for 20 wt% Bi_2O_3 doped ZnO targets. (b and c) HRTEM images of nanopowders prepared by SPVD at air pressure $P = 20$ Torr for 20 wt% Bi_2O_3 doped ZnO targets.

The electrical conductivity determined by impedance spectroscopy is reported in Fig. 16 both with measurements performed on Gd doped Ceria (10 mol% Gd_2O_3) for comparison.

The $Bi_{38}ZnO_{58+\delta}$ cubic phase is more than four orders of magnitude less conductive than Gd doped ceria, but the nanocomposite obtained from the ZnO + 23 wt% Bi_2O_3 mixture, is more than one order of magnitude higher.

4. Discussion

4.1. Interpretation of the observations on undoped ZnO nanopowders

It is striking in Fig. 4 to see that the "grain size" increases together with the shape anisotropy of the "grains". The lattice parameter c and the cell volume increase in the same way (see

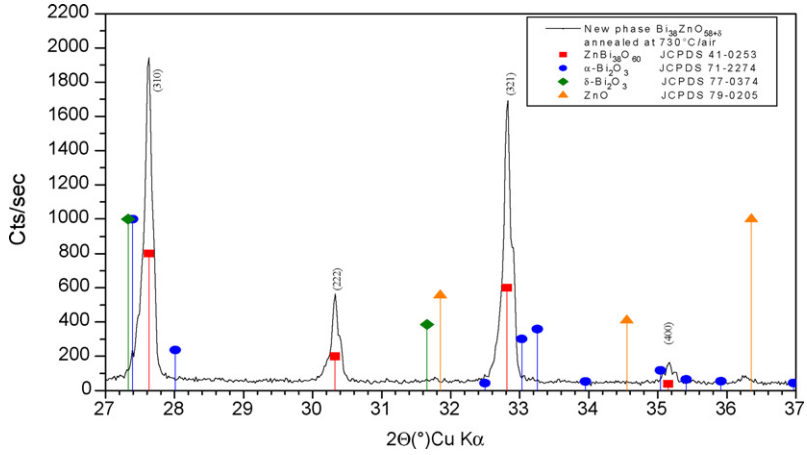

Fig. 15. XRD spectra of $Bi_{38}ZnO_{58+\delta}$ phase showing the absence of isolated ZnO or Bi_2O_3 phases.

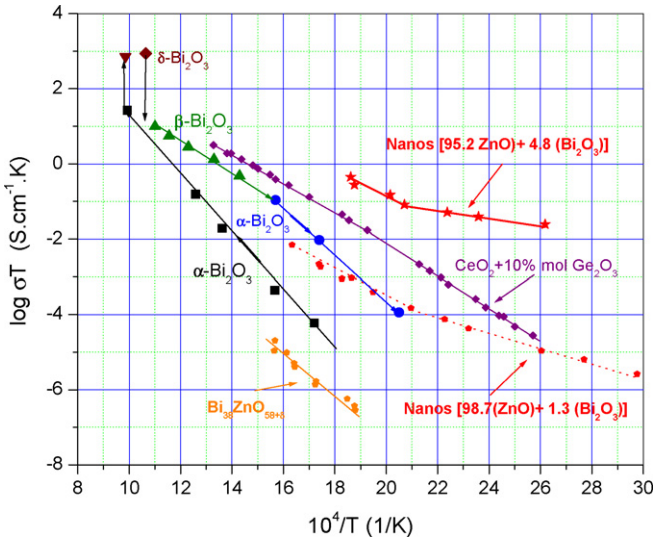

Fig. 16. Arrhenius plot of electrical conductivity of nanomaterials: ZnO + 23 wt% Bi_2O_3 and $Bi_{38}ZnO_{58+\delta}$ synthesized phase are compared to Gd doped CeO_2, and Bi_2O_3 α, β and δ phases.

Fig. 17b and c). An interpretation of these observations seems to be difficult, three possibilities have been nevertheless examined:

- A departure from stoichiometry change with the air pressure.
- An anisotropic stress effect of surface tension linked to the grain shape.
- A substructure effect linked to the anisotropic growth of nanoparticles.

The change in stoichiometry expected from a difference in oxygen partial pressure of about 20 Torr (5–100 Torr air pressure) is not enough large to explain the lattice parameters changes observed.

Anisotropic stresses induced by the surface tension and the grain shape (assumed to be a cylinder in average) could be such that the grain would be in tension along the *c*-axis, that stresses increasing with the shape anisotropy, the radial stresses remaining practically unchanged.

The anisotropic shape of grains is an experimental evidence. It implies a particle growth mechanism in which defects formed in the basal planes: dislocations loops, twins . . . play an important role. The substructure formed can induce strains changing the average distance between planes in the $\vec{c}$ direction, this effect being more important when the nanoparticles are whiskers. TEM observations showing that the whiskers are often slightly twisted (see Fig. 5) and their length is larger than the average "grain size" (in fact the substructure size) determined by XRD, are arguments supporting such a hypothesis.

4.2. *Effect of Bi additions on the ZnO lattice in the nanopowders and nanocomposites*

Additions of Bi have a strong and clear effect on the lattice cell of the solid solution $Zn_{1-y}Bi_yO$ which is the majority phase of the nanopowders.

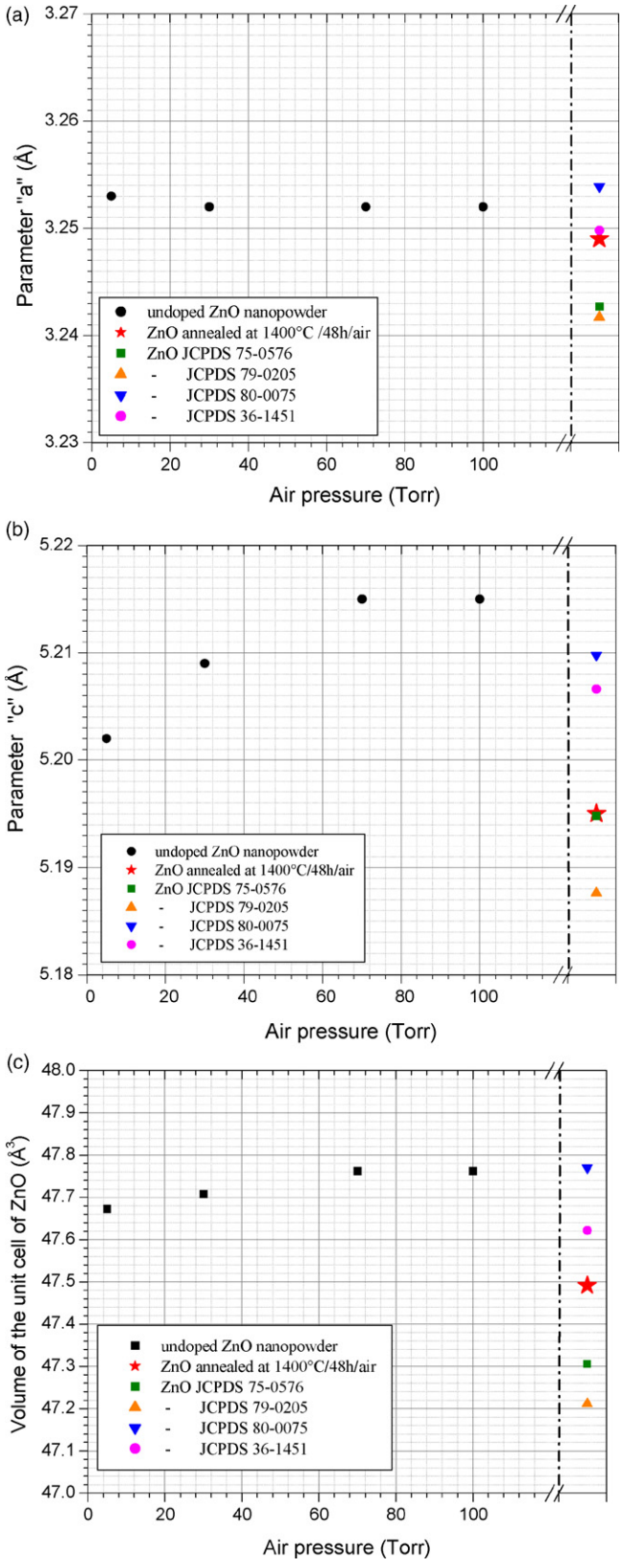

Fig. 17. (a) Lattice *a* parameter variation of ZnO nanopowders as a function of the air pressure inside the solar reactor; right side, reference data. (b) Lattice *c* parameter variation of ZnO nanopowders as a function of the air pressure inside the solar reactor; right side, reference data. (c) Unit cell volume of ZnO nanopowders as a function of the air pressure during the SPVD preparation process; comparison to reference data (values on the right side).

Similarly to pure ZnO nanopowders behaviour (in that case the varying parameter was the oxygen partial pressure) the *c* parameter alone is affected, *a* or *b* parameters remaining practically constant while the composition changes. This last observation is probably due to the fact that the Bi content in the solid solution remains constant, i.e. the solubility limit has been reached.

The influence of Bi additions on the *c* parameter and on the grain size and shape anisotropy is the reverse of that of P_{O2} on pure ZnO nanopowders: the grain size decreases for high Bi content and the anisotropy decreases. These results seem to show that the grains are in compression along the *c*-axis. That could be due to the fact that the secondary phase precipitate mainly in the basal planes. That is supported by Fig. 14a, corresponding to a nanopowder with a high Bi_2O_3 content, showing many precipitates with a six-fold symmetry axis perpendicular to the film.

The solid solution $(Bi_{1-z}Zn_z)_2O_3$ seen in the nanocomposites obtained by sintering Bi doped nanopowders, appears in the phase diagram below 710 °C (see Fig. A1), the peaks of this phase are no significantly shifted compared to pure α-Bi_2O_3 (see Fig. 18). That could indicate the zinc atoms are in interstitial sites. This is supported by the large difference in the ionic radius of Bi^{3+} (1.20 Å) and Zn^{2+} (0.74 Å). Another possibility would be that any zinc atom is dissolved in α-Bi_2O_3 but that would not be in agreement with the phase diagram (see Fig. A1).

4.3. Phase stability and thermokinetic effects

It has been seen in targets that, beside the solid solution $Zn_{1-x}Bi_xO$, appears the $Bi_{38}ZnO_{58+\delta}$ phase which can be written also $(Bi_{1-0.025}Zn_{0.025})_2O_{3-0.1}$ and is close to the δ-Bi_2O_3 cubic phase. In the nanopowders this phase does not appear, but another phase $Bi_{2-u}Zn_{u/2}O_{3-u/2}$ with $u = 0.0875$, close to the β-Bi_2O_3 tetragonal phase, is found (see Fig. 8a and b). The β-Bi_2O_3 phase is not represented in the phase diagram (see Fig. A1), it is not considered generally as stable.

It has been noted that the nanopowders, prepared by SPVD from mixtures of Bi_2O_3 and ZnO, contain two phases (see Section 3.2.2), and that the nanopowders are more Bi rich than the targets. This last result is due to thermokinetic effects and due to the difference between the metallic vapor pressures of the two oxides under air when the oxides sublimate (see Fig. A2). Indeed, literature data on the system ZnO–Bi_2O_3 have been used to compute the vapor pressures of Zn and Bi as a function of the oxygen partial pressure, the diagram of Fig. A2, shows that, while ZnO is more stable than Bi_2O_3, the Bi pressure under $P_{O2} = 0.21$ atm (1 atm air) is slightly higher than the Zn pressure.

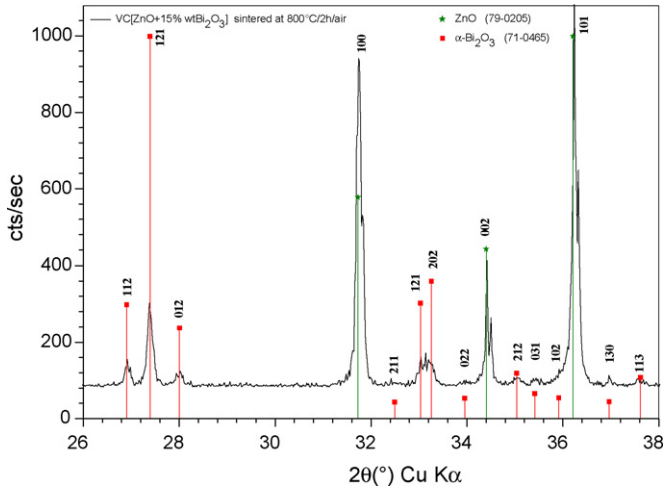

Fig. 18. XRD spectra of sintered nanopowders at 800 °C during 2 h in air.

4.4. Electrical properties

It has been seen that the conductivity of the nanocomposite obtained from the ZnO + 23 wt% Bi_2O_3 nanopowders, is more than one order of magnitude higher than Gd doped ceria.

These nanocomposites are made of two solid solutions: one ZnO rich and the other α-Bi_2O_3 rich. In Fig. 16 the electrical conductivity of the α-Bi_2O_3 phase has been also plotted, it is about three orders of magnitude smaller than the nanocomposite one. A possible explanation of these observations is a composite effect[37,38]: the internal stresses induced by the Bi rich minority phase increase the concentration and the mobility of the points defects responsible for the ionic conductivity.

5. Conclusion

Nanopowders of pure and Bi doped ZnO have been prepared by an original method (SPVD) and their nanostructure characterized by XRD and HRTEM. The Bi doped ZnO nanopowders appear to be formed of two compounds in which cations are in solid solution: $Zn_{1-y}Bi_yO$ close to ZnO and $Bi_{7.65}Zn_{0.35}O_{11.83}$ close to β-Bi_2O_3. The sintering of the nanopowders, producing a massive nanomaterial, leads to a phase change: a compound $(Bi_{1-z}Zn_z)_2O_3$, close to α-Bi_2O_3, appears in place of $Bi_{7.65}Zn_{0.35}O_{11.83}$ close to β-Bi_2O_3.

The nanocomposites obtained from ZnO and Bi_2O_3 mixtures appear to be promising materials for applications such as preparing a new solid electrolyte for SOFC. Nevertheless, new investigations are needed.

Acknowledgement

The authors are grateful to Mr. Boudaren Chaouki, teacher and researcher in Mentouri University at Constantine (Algeria).

Appendix A

A.1. Thermodynamics of the system ZnO–Bi_2O_3

A.1.1. Phase diagram

Fig. A1 shows a phase diagram of the system ZnO–Bi_2O_3 built using data from the literature.[23–26]

It can be noted that the solubility limit of Bi_2O_3 in ZnO is 0.24 mol% or higher at eutectic temperature[23] and the solid solubility of ZnO in Bi_2O_3 occurs[24] at 2.2 mol% near 750 °C.

Up to these compositions, it appears the phase "$24Bi_2O_3{\cdot}ZnO$" and "$Bi_{38}ZnO_{58}$" in the Bi_2O_3 rich side.

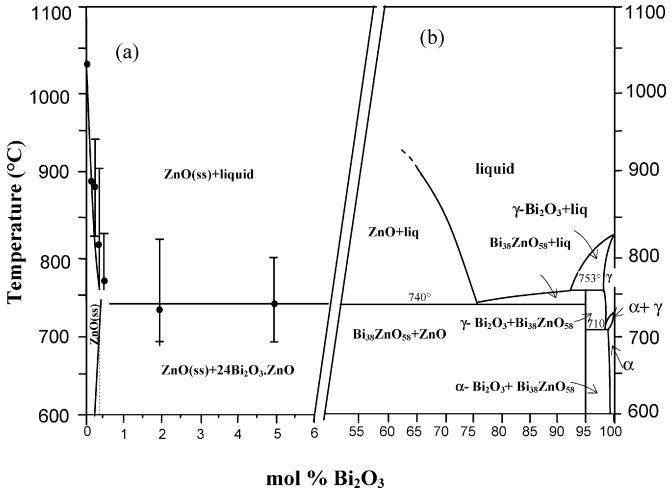

Fig. A1. Binary phase diagram ZnO–Bi_2O_3.[23–26]

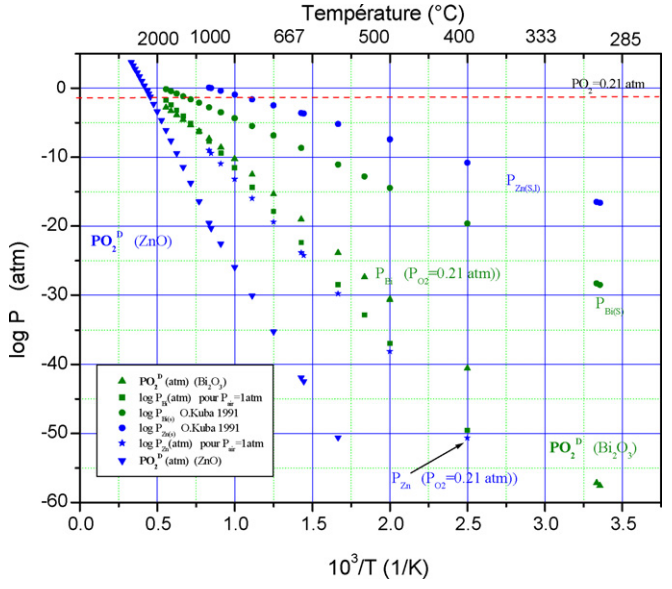

Fig. A2. Arrhenius diagram of metal and oxygen pressure of ZnO and Bi_2O_3 at dissociation equilibrium and under 1 atm air.

It is probably the same phase with different departures from stoichiometry and the general formula can be written: $(Bi_{1-x}Zn_x)_2O_{3+\delta}$, similar to the δ-$Bi_2O_3$ compound.

The metal and oxygen pressures have also been computed at equilibrium (dissociation pressures) and in air using thermodynamic data.[27] The resulting diagram is shown in Fig. A2.

References

1. Michelotti, F., Belardini, A., Rousseau, A., Ratsimihety, A., Schoer, G. and Mueller, J., Use of sandwich structures with ZnO: Al transparent electrodes for the measurement of the electro-optic properties of standard and fluorinated poled copolymers at λ = 1.55 μm. *J. Non-Cryst. Solids*, 2006, **352**(23-25), 2339–2342.
2. Minami, T., Nanto, H., Shooji, S. and Takata, S., The stability of zinc oxide transparent electrodes fabricated by R.F. magnetron sputtering. *Thin Solid Films*, 1984, **111**(2), 167–174.
3. Van De Pol, F. C. M., Thin-film ZnO—properties and applications. *Ceram. Bull.*, 1990, **69**(12), 1959–1965.
4. Yuen, C., Yu, S. F., Lau, S. P. and Chen, G. C. K., Design and fabrication of ZnO light-emitting devices using filtered cathodic vacuum arc technique. *J. Cryst. Growth*, 2006, **287**(1), 204–212.
5. Ohgaki, T., Sugimura, S., Ohashi, N., Sakaguchi, I., Sekiguchi, T. and Haneda, H., Structure and properties of GaN films grown on single crystalline ZnO substrates by molecular beam epitaxy. *J. Cryst. Growth*, 2005, **275**(1–2), e1143–e1148.
6. Jing, L., Xu, Z., Sun, X., Shang, J. and Cai, W., The surface properties and photocatalytic activities of ZnO ultrafine particles. *Appl. Surf. Sci.*, 2001, **180**, 308–314.
7. Zhang, Q., Li, X. and Fujimoto, K., Pd-promoted Cr/ZnO catalyst for synthesis of methanol from syngas. *Appl. Catal. A: Gen.*, 2006, **309**(1), 28–32.
8. Yang, R., Li, Y. and Yu, J., Photo-stabilization of linear low density polyethylene by inorganic nano-particles. *Polym. Degrad. Stab.*, 2005, **88**(2), 168–174.
9. Gordienko, V. P. and Dmitriev, Yu. A., The degradation and stability of polyethylene with small addition of metal oxides under UV-irradiation. *Polym. Degrad. Stab.*, 1996, **53**, 79–87.
10. Matsuoka, M., Non-ohmic properties of zinc oxide ceramics. *Jpn. J. Appl. Phys.*, 1971, **10**(6), 736–746.
11. Gupta, T. K., Applications of zinc oxide varistors. *J. Am. Ceram. Soc.*, 1990, **73**(7), 1817–1840.
12. Levinson, L. M. and Philipp, H. R., Zinc oxide varistors—a review. *Ceram. Bull.*, 1986, **65**, 639–646.
13. Mantas, P. Q. and Baptista, J. L., The barrier height formation in ZnO varistors. *J. Eur. Ceram. Soc.*, 1995, **15**, 605–615.
14. Metz, R., Delalu, H., Vignalou, J. R., Achard, N. and Elkhatib, M., Electrical properties of varistors in relation to their true bismuth composition after sintering. *Mater. Chem. Phys.*, 2000, **63**, 157–162.
15. Xueya, K., Shigen, S., Ying, H. and Minde, T., Influence of ZnO nanometer powders on microstructure and electrical properties of varistor material. *Chin. Mater. Res.*, 1996, **10**(5), 529–535.
16. Xue Ya, K., Yin, H., Ming De, T. and Ming Jing, T., Analysis of ZnO varistors prepared from nanosize ZnO precursors. *Mater. Res. Bull.*, 1998, **33**(11), 1703–1708.
17. Choi, J.-H., Hwang, N.-M. and Kim, D.-Y., Pore-boundary separation behavior during sintering of pure and Bi_2O_3-doped ZnO ceramics. *J. Am. Ceram. Soc.*, 2001, **84**(6), 1398–1400.
18. Peiteado, M., de la Rubia, M. A., Velasco, M. J., Valle, F. J. and Caballero, A. C., Bi_2O_3 vaporisation from ZnO-based varistors. *J. Eur. Ceram. Soc.*, 2005, **25**, 1675–1680.
19. Ait Ahcene, T., Djemel, A. and Monty, C., Elaboration, caractérisation des poudres nanométriques d'oxyde de zinc. *Leban. Sci. Res. Rep.*, 1998, **3**(4), 47–52.
20. Rouanet, A., Sibieude, F. and Monty, C., Production of nanomaterials using highly concentrated solar radiations. *J. Phys. IV Fr.*, 1999, **9**(pr3), 457–462.
21. Onreabroy, W., Sirikulrat, N., Brown, A. P., Hammond, C. and Milne, S. J., Properties and intergranular phase analysis of ZnO–CoO–Bi_2O_3 varistor. *Solid State Ionics*, 2006, **177**, 411–420.
22. Medernach, J. W. and Snyder, R. L., Powder diffraction patterns and structures of the bismuth oxides. *J. Am. Ceram. Soc.*, 1978, **61**(11–12), 494–497.
23. Hwang, J.-H., Mason, T. O. and Dravid, V. P., Microanalytical determination of ZnO solidus and liquidus boundaries in the ZnO–Bi_2O_3 system. *J. Am. Ceram. Soc.*, 1994, **77**(6), 1499–1504.
24. Guha, J. P., Kunej, Š. and Suvorov, D., Phase equilibrium relations in the binary system Bi_2O_3–ZnO. *J. Mater. Sci.*, 2004, **39**, 911–918.
25. de la Rubia, M. A., Fernandez, J. F. and Caballero, A. C., Equilibrium phases in the Bi_2O_3-rich region of the ZnO–Bi_2O_3 system. *J. Eur. Ceram. Soc.*, 2005, **25**, 2215–2217.
26. Peigney, A. and Rousset, A., Phase transformation and melting effects during the sintering of bismuth-doped zinc oxide powders. *J. Am. Ceram. Soc.*, 1996, **79**(8), 2113–2126.
27. Kubaschewski, O. and Alcock, C. B., *Metallurgical Thermochemistry* (*5th ed.*). Pergamon Press, Oxford, 1979, p. 360–384.
28. Bragg, L., *The Crystalline State*, *Vol 1*. G. Bell Londres, 1949.
29. Langford, J. I. and Louër, D., Applications of total pattern fitting to a study of crystalline size and strain in zinc oxide powder. *Powder Diffr.*, 1986, **1**(3), 211–221.

30. De Keijser, Th. H., Langford, J. I., Mettemeijer, E. J. and Vogels, A. B. P., Use of the Voigt function in a single line-method for the analysis of X-ray diffraction line broadening. *J. Appl. Cryst.*, 1982, **15**, 308–314.
31. Garcia-Martinez, O., Rojas, R. M., Vila, E. and Martin de Vidales, J. L., Microstructural characterization of nanocrystals of ZnO and CuO obtained from basic salts. *Solid State Ionics*, 1993, **63**, 442–449.
32. Leung, Y. H., Djurišić, A. B., Gao, J., Xie, M. H. and Chan, W. K., Changing the shape of ZnO nanostructures by controlling Zn vapor release: from tetrapod to bone-like nanorods. *Chem. Phys. Lett.*, 2004, **385**, 155–159.
33. Wu, R., Wu, J., Xie, C., Zhang, J. and Wang, A., Morphological characteristic of Zn/ZnO nanopowders and the optical properties. *Mater. Sci. Eng. A*, 2002, **328**, 196–200.
34. Chen, Z., Shan, Z., Cao, M. S., Lei, L. and Mao, S. X., Zinc oxide nanotetrapods. *Nanotechnology*, 2004, **15**, 365–369.
35. Liu, F., Cao, P. J., Zhang, H. R., Li, J. Q. and Gao, H. J., Controlled self-assembled nanoaeroplanes, nanocoms, and tetrapod-like networks of zinc oxide. *Nanotechnology*, 2004, **15**, 949–952.
36. Wang, B., Zhou, Z. and Gu, L., Influence of tetrapod-shaped zinc oxide whisker on poly (Vinylidene fluoride) based gel polymer electrolyte. *Mater. Res. Bull.*, 2003, **38**, 1449–1455.
37. Shahi, K. and Wagner Jr., J. B., Effect of homovalent ion substitution on phase transformations and conductivity in ionic solid solutions. *Solid State Ionics*, 1984, **12**, 511–516.
38. Chowdhary, P., Tare, V. B. and Wagner Jr., J. B., Electrical conduction in AgI–Al_2O_3 composites. *J. Electrochem. Soc.*, 1985, **132**, 123–124.